galaxies

MDPI

Article

Flattened Galaxy Rotation Curves in the Exochronous Metric

Robin Booth

Astronomy Centre, School of Mathematical and Physical Sciences, University of Sussex, Brighton BN1 9QH, UK; robin.booth@sussex.ac.uk

Abstract: We examine some of the consequences of the Exochronous (timeless) metric and the associated ΣGR cosmological model for the formation of galaxies, and, in particular, their characteristic rotation curves. We show how the cumulative curvature from the multiple spatial hypersurfaces in this model leads to a modified version of the Poisson equation, in which the gravitational potential is computed over 4D space. Using this new form of the Poisson equation, we derive an analytic expression for gravitational potential as a function of radial distance for a uniform gas cloud undergoing gravitational collapse. We show that this results in a radial velocity profile that provides an excellent fit with commonly observed galaxy rotation curves, and hence fully accounts for the effects previously ascribed to dark matter. An expression can be derived for the equivalent matter density profile corresponding to the ΣGR gravitational potential, from which it is evident that this is very similar in form to the well-known Navarro–Frenk–White profile. As a further illustration of the consequences of adopting the Exochronous metric, we show how the principle can readily be incorporated into particle-mesh N-body simulations of large-scale structure evolution, using a relaxation solver for the solution to the Poisson equation and the evolution of the gravitational potential. Examples of the use of this simulation model are shown for the following cases: (a) the initial evolution of a large-scale structure, and (b) galaxy formation from a gravitationally collapsing gas cloud. In both cases, it is possible to directly visualise the build-up of the gravitational potential in 3D space as the simulation evolves and note how this corresponds to what is currently assumed to be dark matter.

Keywords: dark matter; galaxy rotation curves; NFW profile; gravitational potential

check for updates

Citation: Booth, R. Flattened Galaxy Rotation Curves in the Exochronous Metric. *Galaxies* **2024**, *12*, 21. https://doi.org/10.3390/galaxies12030021

Academic Editor: Lorenzo Iorio

Received: 25 February 2024
Revised: 11 April 2024
Accepted: 20 April 2024
Published: 24 April 2024

Copyright: © 2024 by the author. Licensee MDPI, Basel, Switzerland. This article is an open access article distributed under the terms and conditions of the Creative Commons Attribution (CC BY) license (https://creativecommons.org/licenses/by/4.0/).

1. Introduction

The so-called ΛCDM 'Concordance Model' of cosmology is currently our best attempt to describe the origin, evolution, and dynamics of the universe. (See [1] for an overview). There is considerable prima facie evidence to support the main constituents of this model, namely 'dark energy' in the form of a cosmological constant (Λ), and cold non-baryonic 'dark matter'. However, this model is not without problems. Indeed, the continuing inability of the scientific community to identify the origins of dark energy and dark matter arguably constitute the two biggest unresolved questions in physics today.

1.1. Dark Matter

The history of dark matter dates back to 1933, when its existence was inferred by Zwicky from the dynamics of galaxy clusters (see [2], for example). Since then, evidence for the pervasive presence of dark matter has become overwhelming. Detailed accounts of the history of dark matter are provided in [3,4]. One of the most compelling pieces of evidence for dark matter comes from observations of galaxy clusters. These massive structures are made up of hundreds or even thousands of galaxies, and are held together by gravity. When the masses of these clusters are measured using the motions of their galaxies, one finds that there is not enough visible matter to account for the observed motions. This suggests that there must be some additional, invisible, mass present—the so-called dark

matter. Another piece of evidence comes from the cosmic microwave background radiation (CMB), which is the afterglow of the Big Bang. The CMB is almost perfectly uniform, but there are tiny fluctuations in temperature that reveal the distribution of matter in the early universe. These fluctuations can only be easily explained if there is a large amount of dark matter present. There are many other lines of evidence that support the existence of dark matter, including observations of galaxy rotation curves, gravitational lensing, and large-scale structure formation. All of these observations suggest that there is a large amount of invisible mass in the universe that interacts only through gravity. One final argument for the existence of dark matter is provided by an analysis of the total energy manifest of the universe. An analysis of the most recent Planck dataset [5] gave a value for $\Omega_m = 0.315$, with a spatial curvature of zero, implying that $\Omega_{tot} = 1$ and that $\Omega_\Lambda = 0.69$. However, astronomical observations are only able to identify sufficient baryonic matter to account for $\Omega_b = 0.045$, which implies that dark matter is required to contribute the balance, such that $\Omega_{\mathrm{DM}} = 0.26$.

1.2. Galaxy Rotation Curves

There exist many references in the published literature to the phenomenon of anomalous galactic rotation curves, and the implications for the existence of dark matter. (See [6], for example, for a pedagogical overview.) The issue can be summarised reasonably succinctly: the observed velocities of stars orbiting in galaxies, instead of falling off in proportion to $1/\sqrt{R}$ (where R is the radial distance of the star from the galactic centre), as might be expected with a conventional Keplerian model in Newtonian gravity, appear to remain virtually constant and extend out to distances several times greater than the radius of the galaxy's luminous core. This phenomenon appears to be ubiquitous to all observable galaxies. Figure 1 illustrates a typical collection of galaxy rotation curves, using data from [7]. Although various theories have been put forward to explain these anomalous rotation curves, including MOND [8] and other modified gravity theories such as the metric-skew-tensor-gravity (MSTG) theory described in [9], the currently favoured explanation is that of non-baryonic dark matter (NBDM). Not only does this solution provide a good fit with observation, but it is also consistent with the behaviour of other large-scale cosmological phenomena, such as galaxy clustering. A detailed comparison of the respective merits of the NBDM and MOND approaches to explaining galaxy rotation curves is provided in [10]. An even more in-depth review of MOND and several competing models is presented in [11], which also discusses the various predictions made by each model and describes the tests that any alternative model needs to pass in order to be considered a viable theory.

The effect of including a dark matter halo as one of the components of the mass distribution in a typical galaxy is depicted in the plots of Figure 2. This shows that the contributions to the galaxy's gravitational potential arising from the galaxy's central bulge and extended disk give rise to a potential that falls off with increasing distance from the galaxy's centre (dashed orange line). The addition of a dark matter halo results in a virtually flat rotation curve extending out to the visible limits of the galaxy and beyond (solid blue line).

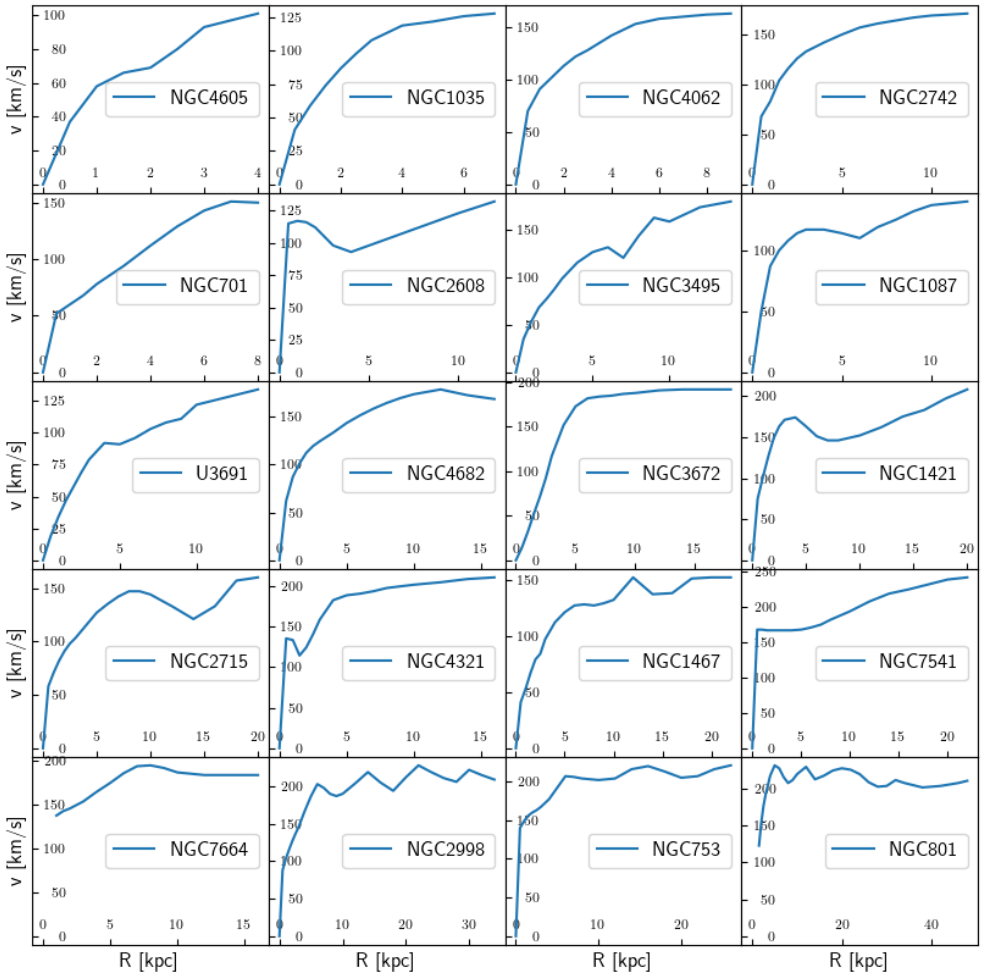


Figure 1. Galaxy rotation curves from observations of 20 galaxies reported in [7].

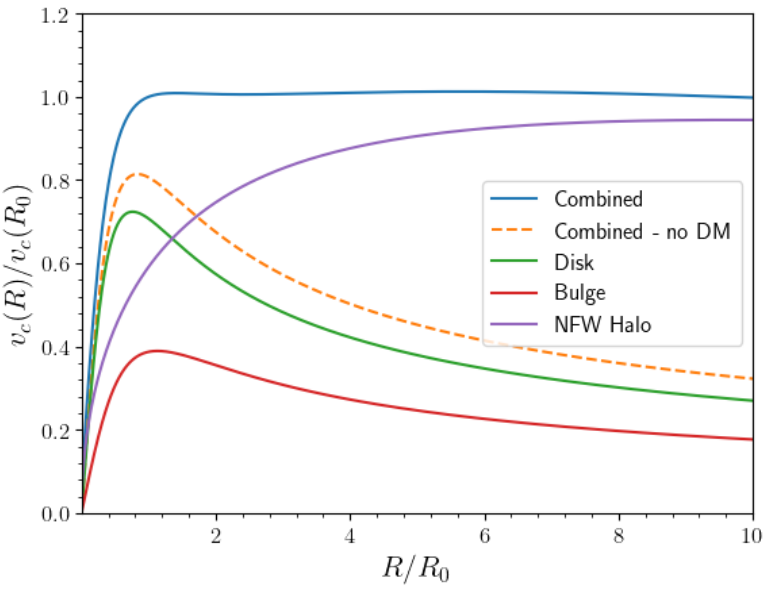


Figure 2. Galaxy rotation curves. The solid blue line shows the flat galaxy rotation curve resulting from the potentials contributed by baryonic matter in the galaxy core and disk and the dark matter in the galaxy's halo. The dashed orange line is the rotation curve that would be observed in the absence of dark matter.

1.3. N-Body Simulations

Observational data are not the only evidence for the presence of dark matter in galactic halos. Results from numerous N-body simulations suggest that dark matter aggregates into halos with a characteristic density profile, the Navarro–Frenk–White (NFW) profile [12], as illustrated in Figure 3.

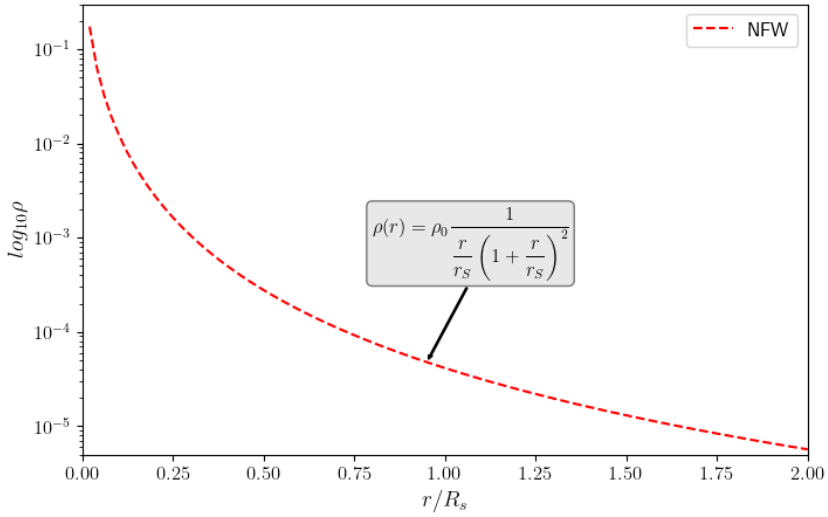


Figure 3. NFW density profile.

Although an NBDM halo exhibiting an NFW density profile is found to be in good agreement with astronomical observations, it remains unclear how this matter distribution arises. A detailed analysis of this problem is provided in [13], which examines the various possible mechanisms for structure evolution within dark matter halos, including the formation of galaxies. The authors note that (as of 2011) numerical simulations have yet to be able to model the formation of a pure disk within a cold dark matter halo, and speculate that this could reflect problem with the standard cosmological paradigm.

In this paper, our objective is to describe an analytical model that is able to accurately account for the observed galaxy rotation curves. In Section 2, we summarise the main elements of the ΣGR paradigm, derived from the Exochronous metric described in [14]. Section 3 derives an equation for the gravitational profile generated by the progressive collapse of a primordial gas cloud to form a galaxy in the context of ΣGR gravity. In Section 4, we apply the new rotation curve formula to the observed rotation curves from a number of galaxies to assess the quality of their fits. Finally, in Section 6, we review the implications of this model in terms of the search for dark matter.

2. The Exochronous Metric

We now examine how a universe based on the Exochronous metric described in [14] can give rise to behaviour that mimics the effects of dark matter, including extended flat galaxy rotation curves, without there being any actual dark matter present. The Exochronous metric replaces the familiar time dimension found in the FLRW metric with a hyperspatial ordering dimension, similar in principle to the concept of a configuration superspace in [15]. This superspace can be thought of as containing multiple foliations of three-spaces, each representing successive configurations of matter and/or quantum fields, as depicted in Figure 4.

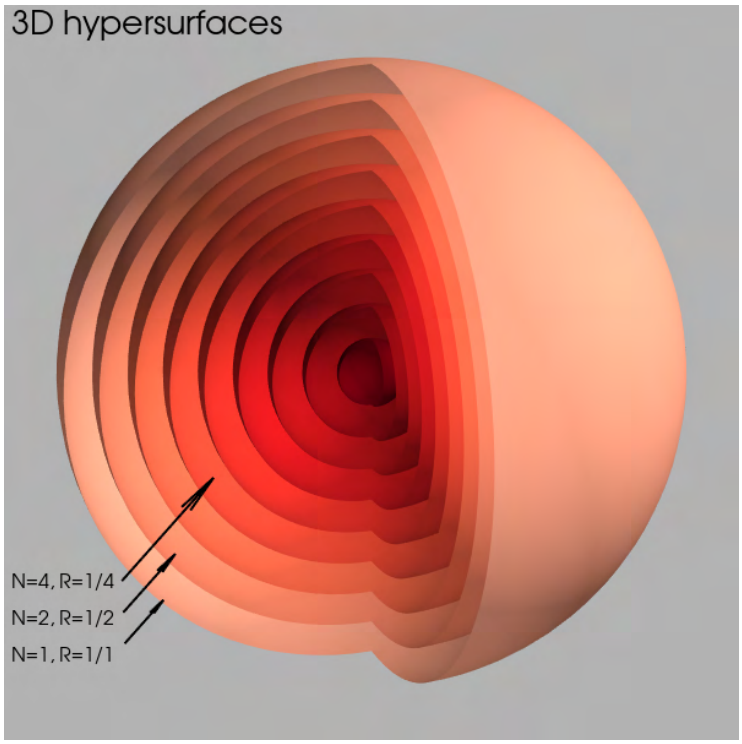


Figure 4. Metric foliations.

The key feature of this configuration superspace, in contrast to the spacetime of GR, is that it contains the cumulative histories of the metric. To illustrate this concept using a visual metaphor, consider the bending of spacetime due to a matter field. With the notion of a time dimension in standard GR spacetime, this curvature will evolve over time as the configuration of the matter field changes, and all traces of its past configuration will be erased (ignoring for now the concept of gravitational waves). This is illustrated by the successive snapshots in Figure 5a.

Contrast this picture with the one illustrated in Figure 5b, where the time dimension is replaced by the ordering dimension in configuration superspace, w. Now, we see that the curvature of the metric induced by the evolving matter field leaves a permanent imprint on the three-space slice. The cumulative effect is that of an aggregation of successive metric deformations, *all* of which contribute to the gravitational mass associated with the matter field that originally gave rise to this deformation.

If we now project the 4D configuration space onto conventional 3D space, we can see that, in the case of a matter field that is shrinking in size, the historic effects of the field on the fabric of space extend well beyond the present-day confines of the field, as illustrated in Figure 5c.

The implication of this reinterpretation of spacetime is that the gravitational potential ϕ arising from a body of matter (or indeed energy) is dependent on the sum of the matter density ρ over each metric foliation, w:

$$\phi(\mathbf{x}, w) \propto \sum_{w=1}^{n} \rho(\mathbf{x}) \tag{1}$$

This sum-over-foliations feature is the reason why we have termed this the ΣGR model. In principle, there is no reason why this model should not apply irrespective of the scale of the matter fields involved. In Section 3, we examine the application of the ΣGR model on large scales: the evolution of galaxies.

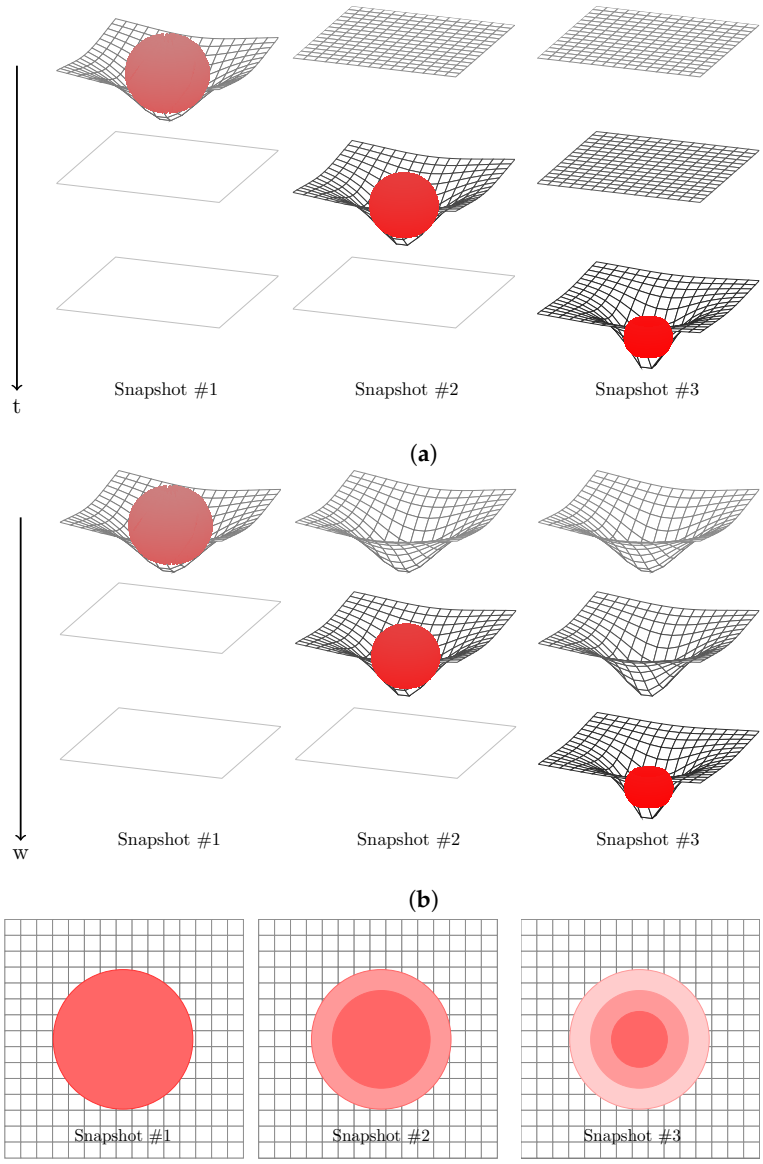


Figure 5. The Exochronous metric. (**a**) Standard spacetime. (**b**) Exochronous superspace. (**c**) Superspace projection onto 3D space.

3. The Galaxy Halo Gravitational Potential Profile

3.1. The Modified Poisson Equation

The Lagrangian density for Newtonian gravity is given by

$$\mathcal{L}(\mathbf{x},t) = -\rho(\mathbf{x},t)\Phi(\mathbf{x},t) - \frac{1}{8\pi G}(\nabla\Phi(\mathbf{x},t))^2 \tag{2}$$

Varying the Lagrangian with respect to x, t gives

$$\delta\mathcal{L}(\mathbf{x},t) = -\rho(\mathbf{x},t)\delta\Phi(\mathbf{x},t) - \frac{2}{8\pi G}(\nabla\Phi(\mathbf{x},t)) \cdot (\nabla\delta\Phi(\mathbf{x},t)) \tag{3}$$

from which we obtain Gauss' law:

$$\rho(\mathbf{x},t) = \frac{1}{4\pi G}\nabla \cdot \nabla\Phi(\mathbf{x},t) \tag{4}$$

which in turn gives us Poisson's equation for gravity:

$$\nabla^2\Phi(\mathbf{x},t) = 4\pi G\rho(\mathbf{x},t) \tag{5}$$

So, in order to calculate the potential arising from a matter distribution that extends over the three spatial dimensions and the hyperspatial dimension of the Exochronous metric, we need to perform the double integral, incorporating Equation (1):

$$\Phi(r,w) = -\frac{4\pi G}{r}\int_0^r \int_0^w r'^2\rho(r',w')dw'dr' \tag{6}$$

where w denotes the foliation index in Exochronous hyperspace.

3.2. Calculating the Galaxy's Gravitational Potential Profile

We now construct a 'toy model' to enable us to calculate the gravitational potential generated by a typical galaxy during its initial formation and subsequent evolution. Consider a spherical gas cloud of initial radius R_0 and initial top-hat density ρ_0 as depicted in Figure 6. Over time, this cloud will progressively collapse under its own gravitational attraction, with an increasing density given by

$$\rho(w) = \rho_0\left(\frac{R_0}{r(w)}\right)^3 \tag{7}$$

Note that in the subsequent analysis we are assuming that this density relationship will apply not only to the initial stage of galaxy formation during virialization, but also to the subsequent gravitational contraction of the galaxy in which its size is assumed to evolve as the inverse of the cosmological scale factor.

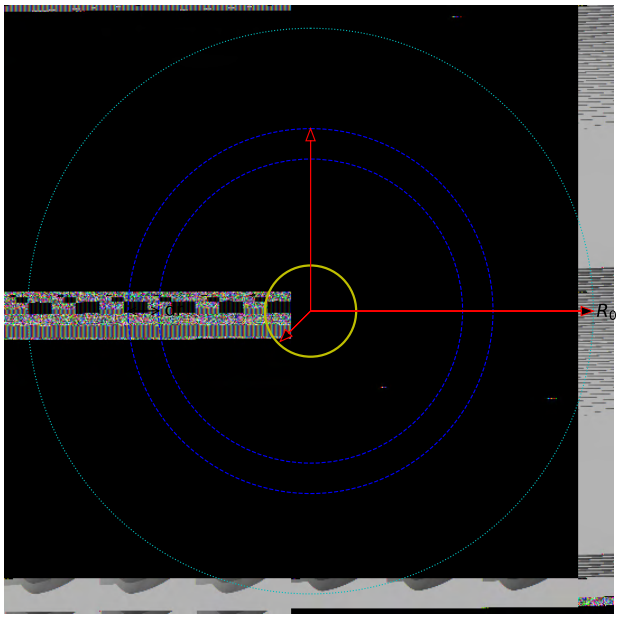


Figure 6. Collapsing gas cloud galaxy model. The galaxy starts with an initial radius R_0 and density ρ_0, and collapses down under gravity to a final core radius, R_c, depicted by the yellow circle. The dashed blue circles depict a spherical shell of gas at radius r from the galactic centre, with a thickness dr.

Recalling from Equation (6) that in Exochronous superspace, the gravitational effects of a body of matter have to be summed over all metric foliations, then for a spherical shell

of gas of thickness dr and at a radius r from the centre of the proto-galaxy we need to calculate the density integral over the w hyperspatial dimension. Thus,

$$\Phi_{\text{shell}}(R, r, w) = -\frac{4\pi G}{R} r^2 \int_{w1}^{w2} \rho(r', w')\, \mathrm{d}w' \mathrm{d}r' \tag{8}$$

For ease of analysis, and in order to make the model independent of any specific timescale, we make two simplifying assumptions:

i The timescale for the initial contraction of the gas cloud to the point where the gas is largely virialized is small in comparison with the time between this point and the present day, and can therefore be neglected in this analysis.

ii The rate of subsequent galaxy contraction (post-virialization) under gravity is linear, such that $\mathrm{d}r/\mathrm{d}w = k$, where k is a constant velocity.

Then, using Equation (7), Equation (8) becomes

$$\Phi_{\text{shell}}(R, r) = -\frac{4\pi G \rho_0 R_0^3}{Rk} r^2 \int_r^{R_0} \frac{1}{r'^3}\, \mathrm{d}r' \tag{9}$$

where R_0 is the initial radius of the proto-galaxy gas cloud. Evaluating Equation (9) gives an expression for the integral of the gravitational potential due to the shell as a function of radial distance R from the galactic centre:

$$\begin{aligned} \Phi_{\text{shell}}(R, r) &= -\frac{4\pi G \rho_0 R_0^3}{2kR} r^2 \left[-\frac{1}{r'^2} \right]_r^{R_0} \\ &= -\frac{2\pi G \rho_0 R_0^3 r^2}{kR} \left(\frac{1}{r^2} - \frac{1}{R_0^2} \right) \end{aligned} \tag{10}$$

Next, we integrate again to give the total potential due to the galaxy halo that lies within a sphere of radius R, but beyond the radius of the visible core R_c:

$$\begin{aligned} \Phi_{\text{halo}}(R) &= -\frac{2\pi G \rho_0 R_0^3}{kR} \int_{R_c}^{R} \left(1 - \frac{r^2}{R_0^2} \right) dr \\ &= -\frac{2\pi G \rho_0 R_0^3}{kR} \left[r \left(1 - \frac{r^2}{3R_0^2} \right) \right]_{R_c}^{R} \\ &= -\frac{2\pi G \rho_0 R_0^3}{kR} \left[R \left(1 - \frac{R^2}{3R_0^2} \right) - R_c \left(1 - \frac{R_c^2}{3R_0^2} \right) \right] \end{aligned} \tag{11}$$

We need to add the gravitational potential due to the galaxy's baryonic core to Equation (11) in order to calculate the total potential at a radial distance R:

$$\Phi(R) = \Phi_{\text{halo}} + \Phi_{\text{core}}$$

In this simple model, we assume that the density ρ_{core} within the core radius R_c is constant, given by

$$\rho_{\text{core}} = \frac{\rho_0 R_0^3}{2k} \left[\frac{1}{R_c^2} - \frac{1}{R_0^2} \right] \tag{12}$$

Hence, the gravitational potential due to the galaxy core becomes

$$\Phi_{\text{core}}(R) = \begin{cases} \dfrac{2\pi G\rho_0 R_0^3 R^3}{3kR}\left[\dfrac{1}{R_c^2} - \dfrac{1}{R_0^2}\right] & \text{for } R < R_c \\ \dfrac{2\pi G\rho_0 R_0^3}{kR}\left[R_c\left(1 - \dfrac{R_c^2}{3R_0^2}\right)\right] & \text{for } R \geq R_c \end{cases} \tag{13}$$

Adding the potential from the galaxy core (Equation (13)) to the potential due to the galaxy halo (Equation (11)) gives us the total potential Φ_{tot} within a sphere of radius R. This is plotted as a function of radial distance in Figure 7, for a range of galaxy core radii, corresponding to successive stages in the galaxy's gravitational collapse. (Note that for the purposes of this exercise, the simplest possible relationship between dr and dw has been assumed, i.e., $k = \mathrm{d}r/\mathrm{d}w = 1$).

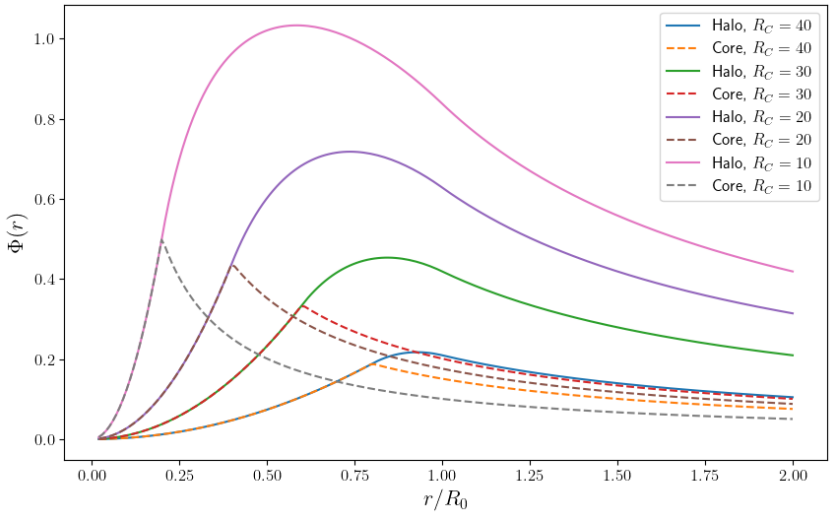


Figure 7. Evolution of the ΣGR potential over a range of galaxy core radii (R_c) as a function of the fraction of initial radius (r/R_0). The dashed lines plot the gravitational potential due solely to the galaxy core. The solid curves show the total potential, including the galaxy halo.

3.3. Effective Density Profile

The foregoing derivation of the dark matter gravitational potential profile and resultant galaxy rotation curve was based on the 4D solution to the Poisson equation. However, we can use the expression for the gravitational potential due to a matter shell in Equation (10) to derive an expression for what might be termed the 'effective density'—in other words, the baryonic matter density that would be required to give rise to this potential. We start with the Poisson equation for gravity—Equation (5)—which for a spherically symmetric source with constant density $\rho = \rho_{\text{eff}} = const.$, with $\Phi = \Phi(r)$ (only r-dependence), can be expressed in spherical coordinates as

$$4\pi G\rho_{\text{eff}} = \frac{1}{r^2}\frac{\partial}{\partial r}\left(r^2\frac{\partial\Phi(r)}{\partial r}\right) \tag{14}$$

where ρ_{eff} is the effective matter density. Rearranging this equation and then integrating both sides gives

$$\partial\left(r^2\frac{\partial\Phi}{\partial r}\right) = 4\pi G\rho_{\text{eff}}r^2\partial\, r$$
$$r^2\frac{\partial\Phi}{\partial r} = \frac{4\pi G\rho_{\text{eff}}r^3}{3}$$
$$\partial\Phi = \frac{4\pi G\rho_{\text{eff}}r}{3}\partial r$$

Solving this differential equation, we obtain

$$\Phi = \frac{2\pi G\rho_{\text{eff}}r^2}{3} \tag{15}$$

Finally, equating this to the formula for the potential $\Phi_{\text{shell}}(R)$ from Equation 10 gives an expression for the shell effective density as a function of the radial distance R from the galactic centre:

$$\rho_{\text{eff}}(R) = \frac{3\rho_0 R_0}{k}\left(\frac{R_0^2}{R^2} - 1\right) \tag{16}$$

This density profile is plotted in Figure 8, together with the NFW profile discussed in Section 1.3. From this, it is evident that the two density profiles are very similar over much of the radial distance range, with the ΣGR density profile diverging as the radial distance approaches the inherent cut-off point when $r = R_0$, whereas the NFW profile extends to infinity. Note the following:

i In practice, it is often useful to take the edge of the NFW halo to be the virial radius, R_{vir}, which is related to the 'concentration parameter', c, and scale radius using $R_{\text{vir}} = cR_s$, where R_{vir} is the radius within which the average enclosed density is $200\times$ the cosmic critical density in standard cosmology.

ii In plotting the density profile of Figure 8, we assumed that $k = 1$. In practice, assuming a linear relationship between dw and dr, then k can be incorporated into ρ_0 as the two parameters are degenerate.

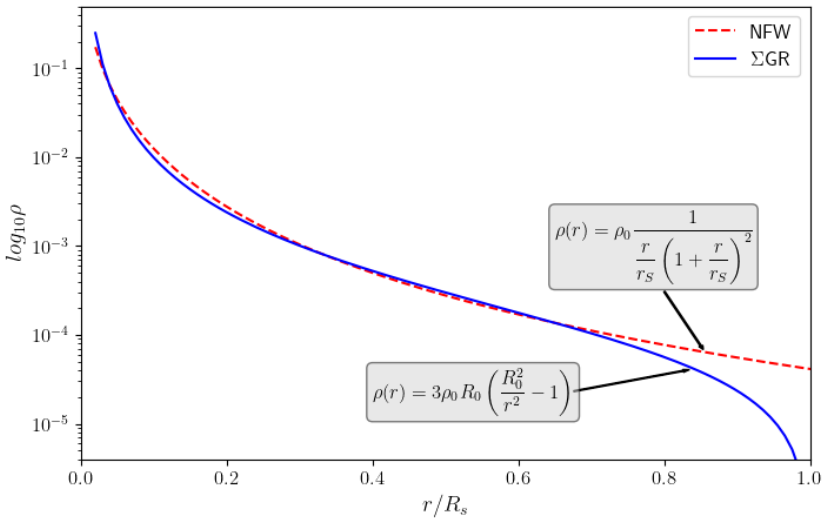


Figure 8. Comparison of the ΣGR effective density profile with the NFW profile.

We can extend this treatment by considering the 'effective mass' due to the galaxy halo. Integrating the effective density, ρ_{eff}, from Equation (16) over the whole spherical volume of the halo from R_c to R_0, we obtain

$$m_{\text{eff}} = \frac{3\rho_0 R_0}{k} \int_{R_c}^{R_0} \frac{4\pi r^2}{3} \left(\frac{R_0^2}{r^2} - 1 \right) \mathrm{d}r \tag{17}$$

$$= \frac{4\pi\rho_0 R_0}{k} \left[r \left(R_0^2 - \frac{r^2}{3} \right) \right]_{R_c}^{R_0}$$

$$= \frac{4\pi\rho_0 R_0}{k} \left(\frac{2R_0^3}{3} - R_0^2 R_c - \frac{R_c^3}{3} \right) \tag{18}$$

We can simplify Equation (18) by replacing R_c with the concentration factor defined as $c \equiv R_c / R_0$, giving

$$m_{\text{eff}} = \frac{4\pi\rho_0 R_0^4}{k} \left(\frac{2 - 3c - c^3}{3} \right) \tag{19}$$

This can be compared to the mass of the galaxy's baryonic core, given by

$$m_{\text{core}} = \frac{4\pi\rho_0 R_0^4}{k} \left(c - c^3 \right) \tag{20}$$

to give an expression for the dark matter to baryon ratio in the galaxy:

$$\frac{m_{\text{dm}}}{m_{\text{bary}}} = \left(\frac{2 - 3c - c^3}{3(c - c^3)} \right) \tag{21}$$

We shall return to this measure at the end of Section 4.

3.4. Rotation Curve

We can use Equation (17) to calculate the cumulative effective mass associated with the galaxy halo, i.e., the equivalent point mass located at the galaxy centre. This is illustrated in Figure 9.

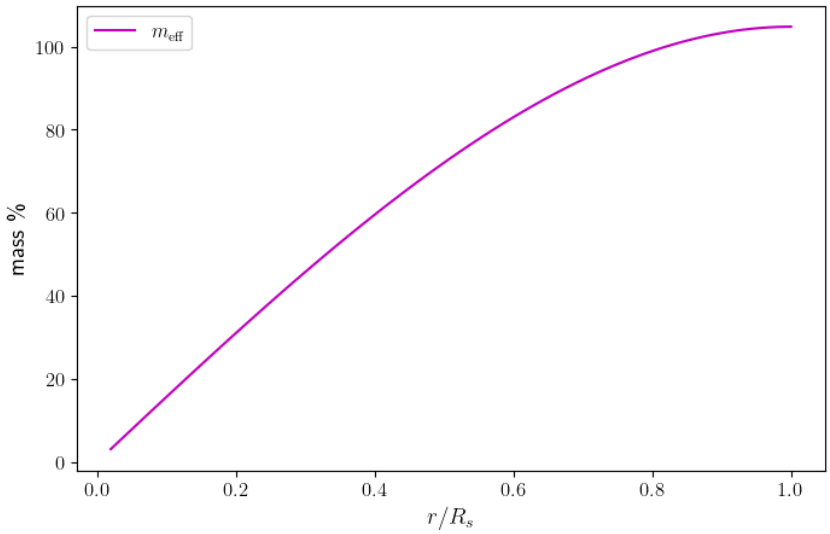


Figure 9. Cumulative effective halo mass as a function of radial distance from centre of galaxy.

Then we can use m_{eff} to calculate the gravitational potential $\Phi(r)$ and hence the orbital velocity using $v^2/r = \nabla\Phi$. The resulting rotation curve for our toy model galaxy is shown in Figure 10, together with the rotation curve that would result from a purely baryonic core.

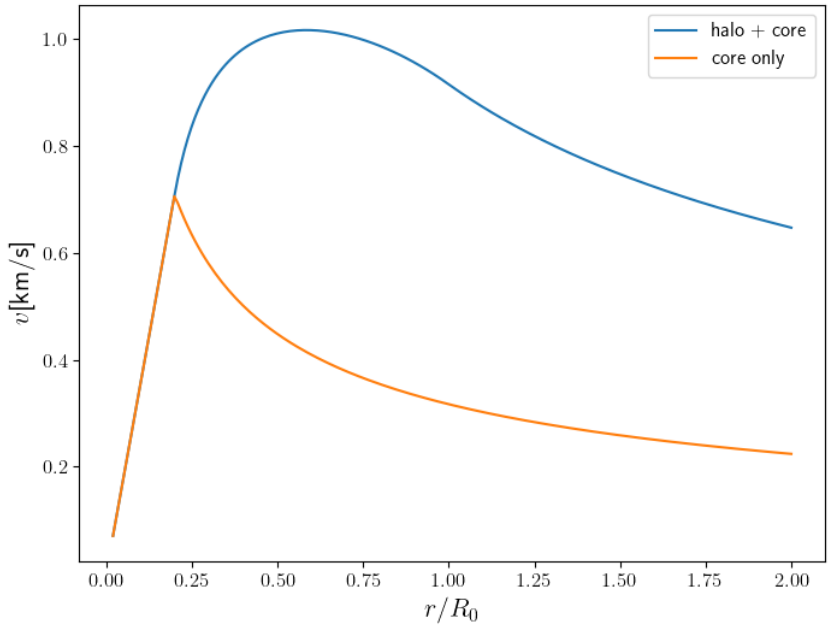


Figure 10. Galaxy rotation curves.

4. Fitting to Observations

The overall shape of the velocity curve in Figure 10 is only dependent on the density–time function. The scale of the curve, in terms of the radial extent and the range of orbital velocities, is determined solely by three parameters: the initial radius of the gas cloud (R_0), the initial density (ρ_0), and the radius of the luminous galaxy core (R_c). Using these three parameters, we can now fit the ΣGR model rotation curve to the observed galactic rotation curves for a sample of galaxies.

For this analysis, we chose to use the sample of galaxies in the Ursa Major cluster provided in [16]. Within this sample, we selected galaxies that meet the criteria of having a minimum of 15 data points spread evenly over the radial distance range, and which also have at least 3 data points within the galactic core region. Figure 11 shows the results of fitting the ΣGR rotation curve model to four of these galaxies.

To explore the relationship between dark matter halo mass and galaxy core baryonic mass, we can take the best fit values for the R_0 and R_c parameters, as listed in the boxes in Figure 11, and use them to calculate the concentration parameter, c, for each of the galaxies in the sample. We can then apply these values to Equation (21) to calculate the galaxy's dark matter to baryon ratio. Note that this ratio is independent of the values of k and ρ_0 used in the fitting exercise. The results are summarised in Table 1.

Table 1. Concentration factor, c, and dark matter/baryon ratio for sample galaxies. Also shown are the 1σ standard deviations for the fitted R_0 and R_c parameters and the R^2 goodness-of-fit score for each curve.

Galaxy	R_0	$1\sigma R_0$	R_c	$1\sigma R_c$	R^2 Fit	c	DM/Baryon
N3877	21.7	1.71	2.50	0.01	0.999	0.12	4.8
N3917	33.6	9.54	3.30	0.11	0.996	0.10	5.8
N4217	19.6	0.76	2.24	0.05	0.996	0.11	4.9
N4100	18.6	0.51	2.97	0.14	0.973	0.16	3.2
Mean						0.12	5.4

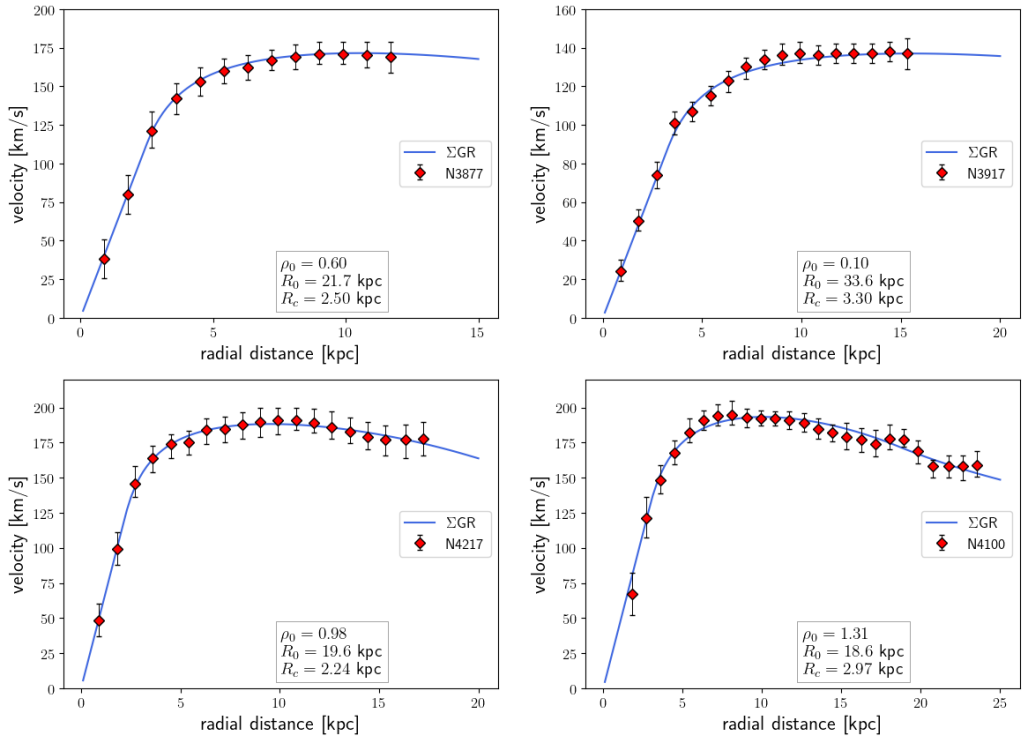


Figure 11. Rotation curves for selected galaxies in the Ursa Major cluster. The figures for ρ_0, R_0, and R_c in the boxes are the best fit parameters for the ΣGR model, and are also summarised in Table 1.

We can compare this ratio with the equivalent results from the most recent Planck CMB dataset [5], which gives estimates for $\Omega_b h^2$ and $\Omega_m h^2$ as 0.0224 and 0.143, respectively, from which we can calculate

$$\frac{\Omega_{dm}}{\Omega_b} = \frac{(\Omega_m h^2 - \Omega_b h^2)}{\Omega_b h^2} = 5.39 \tag{22}$$

The results from the new ΣGR dark matter halo profile formula would therefore appear to be in close agreement with the values previously determined from the Planck data.

5. N-Body Simulation

In addition to validating the ΣGR density profile by fitting to observational galaxy rotation curve data, we can in principle also use the output of N-body simulations as another means of verifying the predictions from this model. However, no existing N-body code currently supports the functionality required to emulate the key feature of the ΣGR model: the ability to solve the Poisson equation in 4D by accumulating the gravitational potential over the course of the simulation run. We therefore took the decision to develop our own simple simulation code to implement the core ΣGR functionality as a proof-of-concept demonstrator.

The decision was made to design the simulation code to be GPU-based. The advantage of this approach is that it becomes possible to run modestly sized simulations extremely fast on relatively inexpensive proprietary hardware; in this case, we used an Nvidia Geforce graphics card. A side benefit of using GPU-based hardware for the simulation is that it can generate on-the-fly video rendering of the simulation output, which greatly simplifies the task of visualising the evolution of a structure within the simulation box. The main features of our simulation code are as follows:

- GUI and control functionality written in C^{++}.
- CUDA C used for the N-body compute kernels.
- The use of a mesh grid for storing (and displaying) the gravitational potential.

- Progressive relaxation solver used for solving the Poisson equation.
- Initial conditions can be generated using Zel'dovich approximation.
- The ability to configure initial overdensity regions, for example when simulating galaxy formation from a gas cloud.
- On-the-fly calculation and display of the following:
  - Matter power spectrum.
  - Velocity curves around a central mass.
- The ability to display gravitational potential as a contour map using the z-axis of the mesh grid.

The main differences between our implementation and conventional N-body simulation codes are as follows:

- The hyperspatial foliation index is used in place of the scale factor as the 'time' coordinate in the simulation.
- Particle accelerations are determined solely by the gravitational potential gradients from the surrounding mesh nodes, and particle–particle interactions are not calculated.
- The Poisson equation does not use any form of FFT solver to calculate long-range potential, and relies exclusively on a relaxation solver.
- The simulation does not incorporate the viscous drag effect that would normally result from implementing the Hubble flow in a co-moving reference frame.
- Gravitational forces are scale-invariant and do not evolve as the simulation progresses.
- Only baryonic matter is used in the simulation (ignoring baryonic particle–particle interactions involving SPH) and *no* dark matter particles are present.

But arguably the key feature that distinguishes this simulation from others is the way in which it implements the cumulative gravitational curvature inherent in the ΣGR model. The relevant line of code from the simulation is

$$\Phi_n = \Phi_{n-1} + 4\pi G\rho_n / r + (\bar{\Phi} - \Phi_{n-1})\tau \tag{23}$$

where Φ_n is the potential of a particular mesh node at time-step n, Φ_{n-1} is the potential at the preceding time-step, ρ_n is the matter density at the node location (calculated using the CiC methodology), $r = 1$ is the mesh grid cell size, $\bar{\Phi}$ is the mean potential arising from the six nodes surrounding the node at the centre of the calculation, and τ is the potential diffusion period, which by determining the speed at which gravitational potential is transmitted across the mesh grid, effectively sets the distance scale of the simulation. Thus, it can be seen that, under this model, the total gravitational potential tracked by the simulation increases without limit over the duration of the simulation. It is this potential, represented by the values at the mesh grid nodes, that is the analog of the Einstein curvature tensor, $G_{\mu\nu}$, but is also what gives rise to the effects that would previously have been ascribed to dark matter in a conventional simulation.

5.1. Large-Scale Structure Formation

We ran the N-body simulation code for a range of simulation box sizes and particle counts in order to verify that the ΣGR model, with an evolving gravitational potential as defined in Equation (23), is capable of generating the range of large-scale structures observed in conventional simulation models without the need for dark matter to be present. Figure 12 shows a snapshot taken from a simulation carried out using a mesh size of 128^3 and 10^7 matter particles. The initial conditions for this simulation were generated by offsetting the particles from their initial positions on a Cartesian grid using the Zel'dovich approximation [17]. The initial matter power spectrum was generated by the CAMB [18] Boltzman solver, with a starting redshift of $z = 70$. This image clearly illustrates the range of large-scale features encountered in standard simulations, including filaments, platelets, and voids.

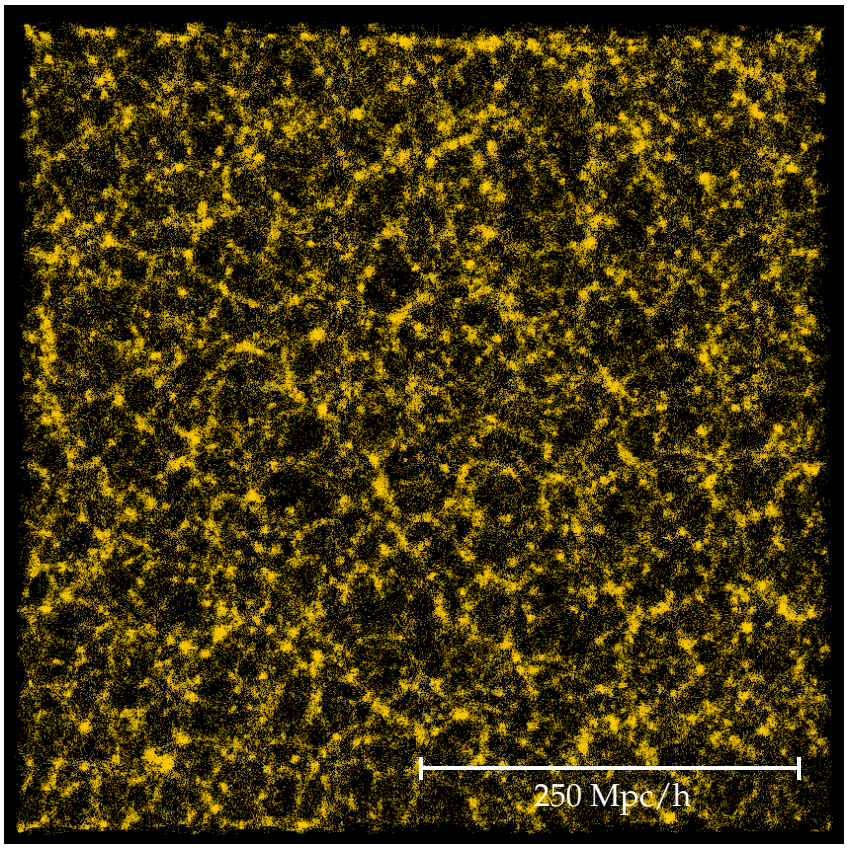


Figure 12. Snapshot from N-body simulation, showing typical "Cosmic web" structure, including filaments, clusters, and voids.

The simulation code has the ability to display the gravitational potential corresponding to a 2D slice as a contour map through a simulation snapshot, using the z-axis to depict the field strength. This is illustrated in Figure 13, which clearly shows the peaks corresponding to clusters of matter, and the extended gravitational field that takes the place of dark matter.

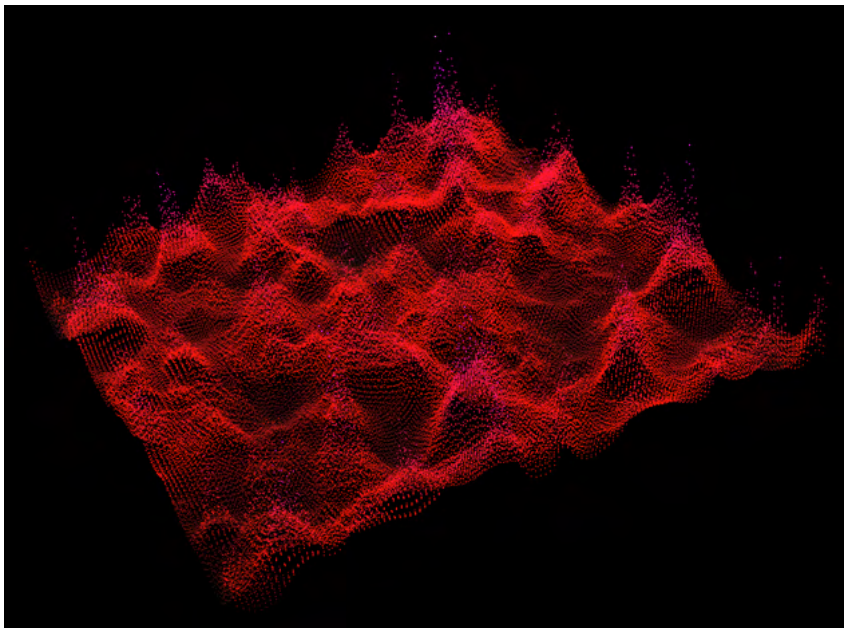
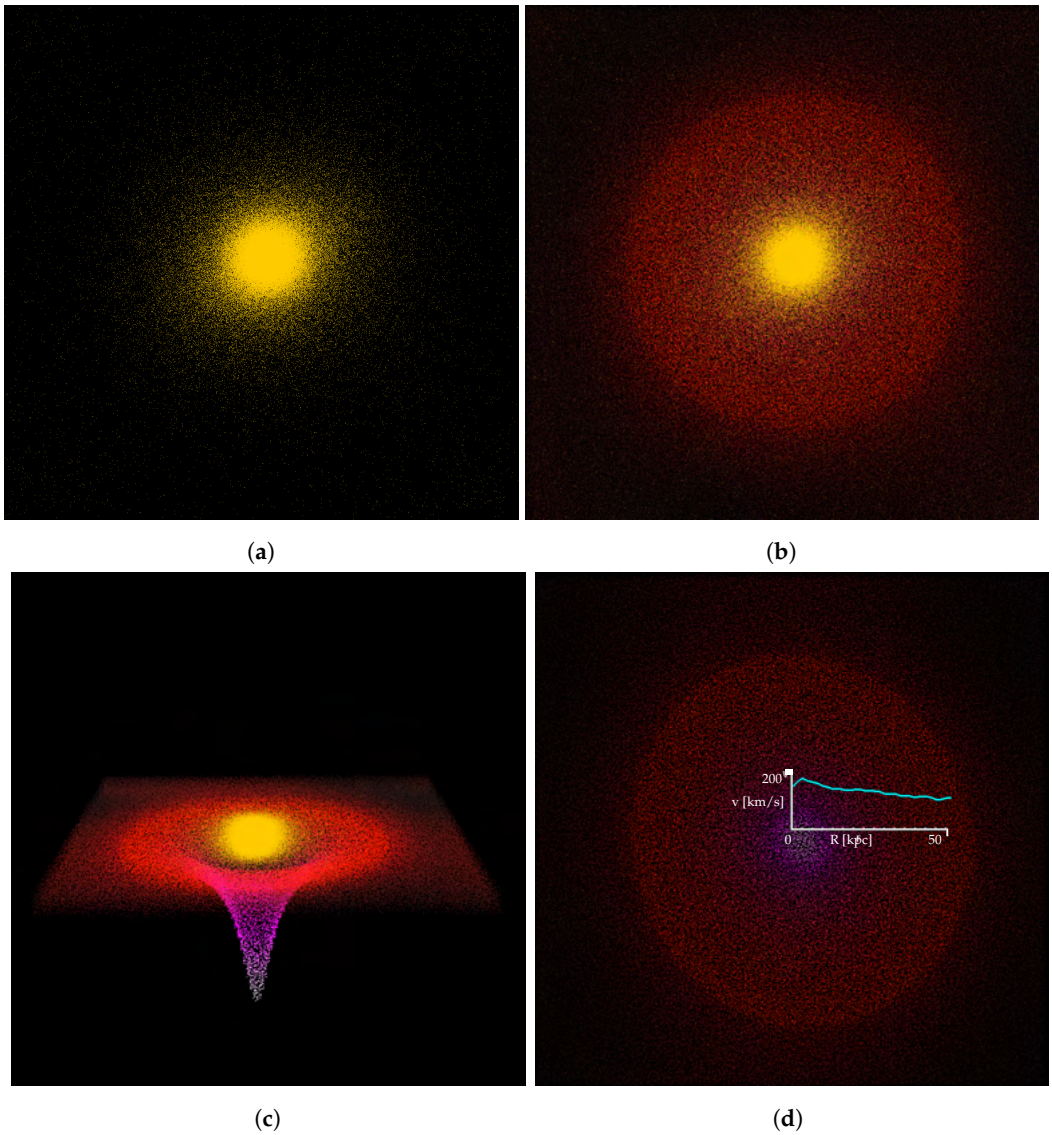


Figure 13. A contour plot of the gravitational potential for a 2D slice though the simulation volume.

5.2. Galaxy Rotation Curve

We also wished to ascertain whether the ΣGR simulation code could mimic the effects of dark matter on galactic scales by simulating the gravitational potential arising from the collapse of a primordial gas cloud, as described in Section 3.2. This was achieved by imposing a spherical top-hat matter overdensity on the initial particle distribution in the simulation, then allowing the simulation to run. The expected behaviour was observed: the matter particles collapsed into the centre of the matter overdensity and their gravitational potential energy was converted into kinetic energy until the ensemble was fully virialized. The visualisation features of the simulation code allow various features of the resultant 'galaxy' to be examined, as illustrated in Figure 14.



(**a**) (**b**)

(**c**) (**d**)

Figure 14. Galaxy formation. (**a**) Elliptical galaxy from collapsing gas cloud. (**b**) Gravitational 'halo' surrounding galaxy. (**c**) Three-dimensional gravitational potential. (**d**) Halo plus rotation curve overlay.

In Figure 14a, we can see the virialized baryonic core of the elliptical galaxy. Figure 14b shows the potential halo surrounding the baryonic core (which extends as far as the initial matter overdensity). We can visualise the 3D gravitational potential surrounding the galaxy by taking a 2D slice though the simulation grid and using the z-axis to represent the gravitational field strength, as illustrated in Figure 14c. The simulation code is capable

of calculating a range of aggregate particle statistics for each simulation snapshot. In Figure 14d, we see a plot of particle velocity as a function of radial distance, over-plotted on the 2D gravitational potential (with the galaxy core hidden), which exhibits the flattened rotation curve that would previously have been ascribed to the presence of dark matter in the galaxy halo.

6. Discussion

In Section 3, we show that it is possible to derive an analytical expression for the gravitational potential profile surrounding a galaxy, based on a collapsing gas cloud model in the context of the Exochronous metric and ΣGR gravity, and we show that this is very similar to the potential associated with the well-known NFW profile. In Section 4, we demonstrate that the rotational velocity curves generated using this gravitational field profile can be accurately fitted to the observed rotation curves obtained from a sample of spiral galaxies. From this curve fitting exercise it is evident that, in spite of the simplifying assumptions made in respect of galaxy contraction rates and core density, the ΣGR model is able to account very precisely and predictably for the observed flattened rotation curves. Essentially, what we are seeing is the effects of a galactic halo composed of what might be more accurately termed 'Ghost Matter'—the legacy of layers of gravitationally warped 3D hypersurfaces laid down over time by the primordial galactic gas cloud as it condenses and contracts. It should be noted that the foregoing analysis only concentrates on a small sample of spiral galaxies that have, presumably, followed the simple collapsing gas cloud model used here. However, it is reasonable to expect that the same concept of a galactic gravitational halo will still be applicable to other more complex galactic evolution models, such as, for example, galaxies formed from the merger of two smaller galaxies. The key point to emphasise from this exercise is that the resultant flattened galaxy rotation curves result solely from the action of baryonic matter, with so-called dark matter playing no part in the process.

We developed a simple N-body simulation code designed to reproduce the effects of a cumulative gravitational potential on the evolution of large-scale structures, as described in Section 5. We used this simulation to demonstrate that the ΣGR model can, at least qualitatively, reproduce the effects previously ascribed to dark matter in conventional simulation codes, in terms of observable large-scale features such as platelets, filaments, and voids. We also used this simulation code to model the gravitational collapse of a primordial gas cloud to form a galaxy, and showed that this results in the typical flattened galaxy rotation curve encountered in real-world observations. Again, the main conclusion from this exercise is that the ΣGR model can account for cosmological observations without the need to invoke dark matter. It should, however, be noted that the collapsing gas cloud model described in Section 3 and the N-body simulations reported in Section 5 are both applicable to the epoch where $z < 100$ and hence have no bearing on the presence or absence of dark matter in the universe prior to the epoch of recombination at $z \simeq 1100$ or on the CMB power spectrum.

Funding: This research received no external funding. The APCs associated with this article have been financed by crowdfunding. The author wishes to thank the following donors for their generous patronage: Jessica Booth, Jonathan Evans, Martin Evans, Jonathan Hawkins, Robert Hadfield, Nicholas Norton, and Peter Whittle.

Data Availability Statement: All the data analysed in this article are available from the references cited in the article.

Acknowledgments: The author wishes to thank the anonymous referees for their constructive reports and suggestions, which helped improve the clarity of this article.

Conflicts of Interest: The author declares no conflicts of interest.

References

1. Springel, V.; Frenk, C.; White, S. The large-scale structure of the Universe. *Nature* **2006**, *440*, 1137–1144. [CrossRef] [PubMed]
2. van den Bergh, S. The Early History of Dark Matter. *Publ. Astron. Soc. Pac.* **1999**, *111*, 657–660. [CrossRef]
3. Peebles, P.J.E. Growth of the nonbaryonic dark matter theory. *Nat. Astron.* **2017**, *1*, 57. [CrossRef]
4. Bertone, G.; Hooper, D. History of dark matter. *Rev. Mod. Phys.* **2018**, *90*, 045002. [CrossRef]
5. Aghanim, N.; Akrami, Y.; Ashdown, M.; Aumont, J.; Baccigalupi, C.; Ballardini, M.; Banday, A.J.; Barreiro, R.B.; Bartolo, N.; Basak, S.; et al. Planck 2018 results: VI. Cosmological parameters. *Astron. Astrophys.* **2020**, *641*, A6. [CrossRef]
6. Bahcall, J.; Piran, T.; Weinberg, S. *Dark Matter in the Universe*; World Scientific: Singapore, 2004. [CrossRef]
7. Rubin, V.C.; Ford, W.; Thonnard, N. Rotational Properties of 21 Sc Galaxies with a Large Range of Luminosities and Radii from NGC 4605 (R = 4 kpc) to UGC 2885 (R = 122 kpc). *Astrophys. J.* **1980**, *238*, 471–487. [CrossRef]
8. Milgrom, M. MOND-a pedagogical review. *arXiv* **2001**, arXiv:astro-ph/0112069.
9. Brownstein, J.R.; Moffat, J.W. Galaxy Rotation Curves without Nonbaryonic Dark Matter. *Astrophys. J.* **2006**, *636*, 721. [CrossRef]
10. Hofmeister, A.M.; Criss, R.E. Debated models for galactic rotation curves: A Review and mathematical assessment. *Galaxies* **2020**, *8*, 47. [CrossRef]
11. Banik, I.; Zhao, H. From Galactic Bars to the Hubble Tension: Weighing Up the Astrophysical Evidence for Milgromian Gravity. *Symmetry* **2022**, *14*, 1331. [CrossRef]
12. Navarro, J.F.; Frenk, C.S.; White, S.D.M. The Structure of Cold Dark Matter Halos. *Astrophys. J.* **1996**, *462*, 563. [CrossRef]
13. Diemand, J.; Moore, B. The structure and evolution of cold dark matter halos. *Adv. Sci. Lett.* **2011**, *4*, 297–310. [CrossRef]
14. Booth, R. The Exochronous Universe: A static solution to the Einstein field equations. *arXiv* **2022**, arXiv:2201.13120. [CrossRef]
15. Barbour, J.; Foster, B.; O'Murchadha, N. Relativity without relativity. *Class. Quantum Gravity* **2002**, *19*, 3217–3248. [CrossRef]
16. Verheijen, M.a.W.; Sancisi, R. The Ursa Major cluster of galaxies. *Astron. Astrophys.* **2001**, *370*, 765–867. [CrossRef]
17. Zel'dovich, Ya. Gravitational instability: An approximate theory for large density perturbations. *Astron. Astrophys.* **1970**, *5*, 84–89.
18. Lewis, A.; Challinor, A.; Lasenby, A. Efficient Computation of Cosmic Microwave Background Anisotropies in Closed Friedmann-Robertson-Walker Models. *Astrophys. J.* **2000**, *538*, 473–476. [CrossRef]

Disclaimer/Publisher's Note: The statements, opinions and data contained in all publications are solely those of the individual author(s) and contributor(s) and not of MDPI and/or the editor(s). MDPI and/or the editor(s) disclaim responsibility for any injury to people or property resulting from any ideas, methods, instructions or products referred to in the content.